Comprehensive Analysis of the Fault Inception Angle Influence in Fault-Induced Traveling Waves

S. S. B. Azevedo, R. L. S. França, J. T. L. S. Campos, and F. B. Costa

***Abstract*—This work presents a comprehensive analysis of the fault inception angle influence in the first wavefront of the fault-induced traveling waves (TWs) for all types of faults in a transmission line. The EMTP-ATP software simulated fault-induced TWs for all transmission line fault types considering the JMarti frequency-dependent transmission line model, whereas an emulated transmission line in an experimental setup generated fault-induced TWs of single line-to-ground faults for validating the effects of the fault inception angle. This work demonstrated that the energy of the fault-induced TWs changes with the fault inception angle according to a squared sinusoidal function, and pointed out the situations where there is no TW in each type of fault. Besides the support for a better understanding of fault-induced TWs, the analysis accomplished here will be essential for further development of TW-based detection, location, and protection methods.**

***Keywords*—Traveling waves, fault inception angle, transmission line protection and location.**

I. Introduction

OVERHEAD transmission lines are usually long, and they are subject to vandalism, weather, and environmental conditions. Therefore, about 50% of faults in the electrical power system occur in transmission lines [1]. Several issues are a consequence of fault occurrences, such as loss of stability, damages to system elements, and unavailability of part of the power system. Therefore, it is necessary to clear faults before exceeding the fault clearing time limit, improving power quality and the people's safety and reducing material damage and power losses [2].

The most common transmission line protection schemes, such as overcurrent and distance protections, apply phasor estimation of the fundamental component, which usually requires a power cycle delay time [2]. Additionally, protection of high-voltage lines are subject to errors due to shunt leakage current, current transformer saturation, and decaying-direct-current [3]. All these problems induce procedure errors such as false- or no-trip signals sent to circuit-breakers. TW-based protection schemes are a promising possibility since they are designed to be the fastest ones and are less affected by the aforementioned issues [4].

Besides the protection, the accurate estimating of the fault location is essential, and means fast transmission line recovery, improving the availability and performance of the system [5]. In this context, TWs carry important information about the fault, such as the type of fault and the fault location, which propagates in overhead transmission lines with a velocity close to the velocity of light. Therefore, such information can properly support fast and accurate transmission line protection [4, 6] and automatic fault diagnosis methods, including the fault detection, classification, location, and direction [5, 7–10].

The detection of TWs has limitations mainly due to damped transients, specially for the zero-mode TW since its energy is lower than that for the alpha-mode TW. This can be seen in simulations and in real-world data. Therefore, TW-based detection methods must face this problem. Several mathematical tools have been applied by TW-based detection methods, e.g, principal component analysis [11], mathematical morphology [12], Park's transformation [13], wavelet transform [14], and differentiator-smoother filter [15], which is used in commercial TW-based relays [16]. In addition, the TW32, which is a traveling wave-based directional function applied commercially, requires detection of zero- and alpha-mode by means of the differentiator-smoother filter and has presented good performance [6]. Most of these methods report the challenge of detecting TWs for specific fault inception angles. However, how exactly TWs are affected by the fault inception angle in all types of faults? This question is not well-reported in the literature.

This work presents a comprehensive analysis of the fault inception angle influence in the first wavefront of the fault-induced traveling waves for all types of faults. The EMTP-ATP software simulated fault-induced traveling waves for all transmission line fault types considering the JMarti frequency-dependent transmission line model, whereas an emulated AC transmission line in an experimental setup generated fault-induced traveling waves of single line-to-ground faults for validating the effects of the fault inception angle. It is well-known that there are specific fault inception angles where no traveling waves are generated, termed as critical fault inception angle for TW-based methods. However, this paper demonstrates that the critical fault inception angles are different for all types of faults, and they are a concern in SLG and line-to-line (LL) faults, whereas TWs are always detectable in double line-to-ground (DLG) and three-phase faults because there are relevant TWs in at least on signal based on the fault inception angle parameter. Furthermore, the first wavefront energy of the fault-induced traveling waves changes with the fault inception angle according to a square sinusoidal function. Phase-, zero-, and alpha-mode traveling waves of currents and voltages are evaluated in this paper. Besides the support for a better understanding of fault-induced TWs, the analysis accomplished here will be essential for further developing TW-based detection, location, and protection methods.

This study was financed in part by the Coordenação de Aperfeiçoamento de Pessoal de Nível Superior - Brasil (CAPES) - Finance Code 001 and in part by the Conselho Nacional de Desenvolvimento Científico e Tecnológico - Brasil (CNPq).

S. S. B. Azevedo, R. L. S. França, J. T. L. S. Campos, and F. B. Costa are with Federal University of Rio Grande do Norte (UFRN), Campus Universitário Lagoa Nova, Natal - RN, 59.078-970, Brazil (e-mail: samuazev@gmail.com, rafaellucas@ufrn.edu.br, j.campos893@gmail.com, and flaviocosta@ect.ufrn.br).

Paper submitted to the International Conference on Power Systems Transients (IPST2021) in Belo Horizonte, Brazil June 6-10, 2021.

II. TW Propagation Theory

Faults in transmission lines result in TWs which propagate towards the line terminals at a speed close to the speed of light in overhead lines. Fig. 1 depicts the lattice diagram for a fault on the middle of the line.

When the first wavefronts (v_{I}, i_{I}, v_{II}, and i_{II}) reach the line terminals, some of this energy continues to propagate through the system, as refractions (v_{It} and i_{It}), whereas another part is reflected back toward the fault point (v_{Ir} and i_{Ir}). There, they will again be reflected and refracted. Thus, refractions and reflections will follow, generating waves with less and less energy, until finally, the system reaches equilibrium more than once.

The transmission line topology, as well as the parameters of its conductors, determine the TW propagation velocity, which can be estimated by $v = 1/\sqrt{LC}$, disregarding the losses, where L and C are line distributed inductance and capacitance, respectively. The TW transit time τ along the line is estimated dividing the line length by its velocity. By applying a power invariant transformation, like the Clarke's one, it is possible to obtain the velocities of the aerial (alpha) and earth (zero) propagation modes.

III. The Real-Time Stationary Wavelet Transform

The first-level RT-SWT wavelet coefficients associated with the actual sampling time k/f_s is given by [17]:

$$w(k) = \sum_{n=0}^{\text{L-1}} h_\psi(n) x(k - L + n + 1), \tag{1}$$

where h_ψ are the coefficients of the wavelet filter; x is the sampled signal, which can be a voltage or a current.

The spectral wavelet coefficient energy of the signal x within a Δk-sized sliding window is given by [18]:

$$\varepsilon(k) = \sum_{n=k-\Delta k+L}^{k} [w(n)]^2, \tag{2}$$

where $k \geq \Delta k + 1$; $\Delta k = L$, which allows the fastest extraction of the TWs.

IV. Severity of the First Wavefront of TWs

The wavelet coefficient energy during the first wavefront of the TWs, termed in this paper as the first wavefront energy, is proportional to the energy of this first wavefront. This is true when: 1) the sampling frequency is high enough to isolate only the TWs in the frequency spectrum of the wavelet coefficients, which is from $f_s/4$ to $f_s/2$; 2) the first and second wavefronts take place in a time enough to be distinguished, such as in the best situation which is when the fault occurs on the middle of the line. In this fashion, if the first wavefront is relevant in magnitude, then the first wavefront energy will be strong, whereas if the first wavefront is irrelevant, then the first wavefront energy will present disregarded value.

The first wavefront energy is the area under the wavelet coefficient energy as follows:

$$\lambda = \sum_{n=k_i}^{k_t} \varepsilon_{\mathrm{x}}^{\mathrm{w}}(n) f_{\mathrm{s}}, \tag{3}$$

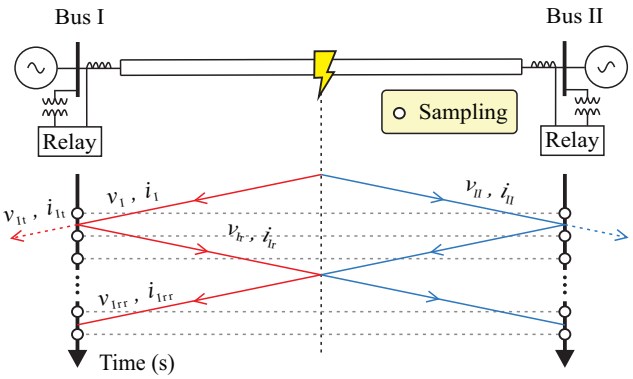

Fig. 1. Lattice diagram.

where k_{i} is the sampling associated to a time just before the first wavefront arrival time and k_{t} is the sampling associated to a time after the first wavefront arrival time, but before the second wavefront arrival time.

Fig. 2 depicts an example to compute the first wavefront energy of a TW. The fault was simulated on the middle of the line, where the time distance between the first and the second wavefronts is one transient time. k_{t}-k_{i} was selected as half transit time τ. k_{fwf} and k_{swf} are the actual sampling of the first and second wavefront arrival time, respectively. Since $k_{\mathrm{t}} < k_{\mathrm{swf}}$, the second wavefront of the TWs was not taken into account.

V. Simulations of TWs

A 60 Hz, 230 kV transmission system shown in Fig. 1 was modeled in the EMTP-ATP. The transmission line with 200 km length, with topology presented in [6], was modeled using the JMarti frequency-dependent line model with ideal transposition and frequency response up to 10 MHz. The paramenters of the source connected to the Bus I are: U = 230.091$\angle$1.536° kV, Z_1 = 2.156 + j11.660 Ω/km, and Z_0 = 11.484 + j31.504 Ω/km, whereas the paramenters of the source connected to the Bus II are: U = 230.053$\angle -$16.460° kV, Z_1 = 2.156 + j11.660 Ω/km, and Z_0 = 11.484 + j31.504 Ω/km, where U, Z_1, and Z_0 are voltage, positive sequence impedance, and zero sequence impedance,

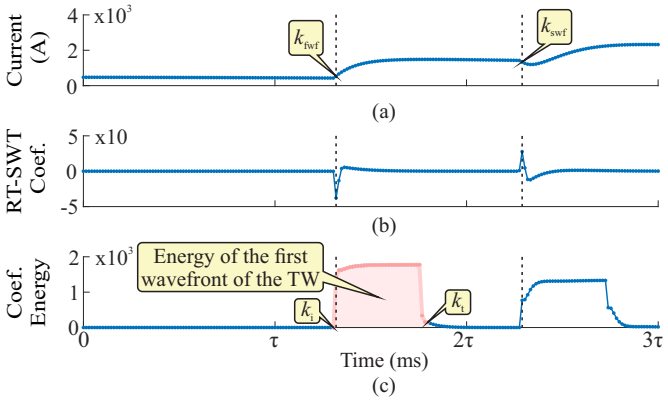

Fig. 2. Computation of first wavefront energy area: (a) current signal; (b) RS-SWT coefficients; (c) RS-SWT coefficients energy.

respectively. A sampling frequency of 1 MHz was adopted. The fault-inception angle was varied from 1 to 360 degrees, at steps of 1 degree. The fault distance was taken in the middle of the transmission line (d_F=100 km) in order to avoid the influence of the second reflection of the TWs in the detection of the first wavefront. The fault resistance was R_f=0 Ω to better highlight the effects of the fault inception angle in the TWs. The alpha-mode velocity was estimated at 99.72% of the speed of light, whereas the zero-mode velocity was about 93.94%. These propagation velocities were estimated with the simulation of a phase A-to-ground fault, at Bus II, with a measurement at Bus I.

A. General Features of the First Wavefront of TWs

Figs. 3, 4, 5, and 6 depict the first wavefront energy of SLG, LL, DLG, and three-phase faults, respectively, in the base-10 logarithmic scale. They were normalized with the maximum first wavefront energy of phase A in phase-A-to-ground (AG) faults: $\max[\lambda_A^{AG}] = 5.36 \times 10^{-4}$. Each figure depicts the first wavefront energy as a function of the fault inception angle for phase-, zero-, and alpha-mode currents at Bus I. The same features were obtained for the voltages, which are not shown in this paper. Specific details about each situation are provided in the next subsections.

The Curve Fitting Toolbox of Matlab® was applied over simulation results aiming the regression analysis of the first wavefront energy as a function of the fault inception angle for all fault types. Therefore, based on the standard Levenberg-Marquardt optimization algorithm, the regression analysis resulted in a formulation of the first wavefront energy λ as a function of the fault inception angle θ_f, as follows:

$$\lambda(\theta_f) = \Lambda_0 + \Lambda_1 sin^2(\theta_f + \delta), \quad (4)$$

where δ is an first wavefront energy shift angle; Λ_0 and Λ_1 are magnitudes of the first wavefront energy, i.e., they indicate the severity of the first wavefront, which change with the fault parameters. The first wavefront energy of the phase currents (λ_A, λ_B, λ_C), the zero-mode current (λ_{Zero}), and alpha-mode current (λ_{Alpha}) measured at Bus I were assessed for each simulation.

According to (4), the first wavefront presents maximum and minimum values at specific fault inception angles according to the type of fault. Table I summarizes the fault inception angles, per type of fault, in which no TWs are generated (critical fault inception angles), according to simulation results. The maximum TWs are generated 90^o after or before each minimum point.

Despite presenting differences, SLG and LL faults have something in common: their first wavefront energy reaches the peak and valley values in the same fault inception angles for all phase-, zero-, and alpha-mode curves. This means that, for certain fault inception angles, the fault-induced TWs are undetectable at any phase, zero-mode or alpha-mode. Conversely, in the case of DLG and three-phase faults, this issue does not occur because, for any fault inception angle, there are at least two phases in which TWs can be detected, even when there are no TWs on either zero- or alpha-modes. Therefore, in theory, TW-based detection methods can detect TWs induced by DLG and three-phase faults for any fault inception angle by using the phase-mode TWs.

TABLE I
(CRITICAL FAULT INCEPTION ANGLES.)

Fault Type	Component				
	A	B	C	Zero	Alpha
AG	0°	0°	0°	0°	0°
	180°	180°	180°	180°	180°
BG	120°	120°	120°	120°	120°
	300°	300°	300°	300°	300°
CG	60°	60°	60°	150°	60°
	240°	240°	240°	240°	240°
AB	150°	150°	All	All	150°
	330°	330°			330°
BC	All	90°	90°	All	All
		270°	270°		
CA	30°	All	30°	All	30°
	210°		210°		210°
ABG	None	None	60°	60°	158°
			240°	240°	338°
BCG	0°	None	None	0°	98°
	180°			180°	278°
CAG	None	120°	None	120°	22°
		300°		300°	202°
ABC	0°	120°	60°	All	0°
	180°	300°	240°		180°

B. Single Line-to-Ground Faults

According to Fig. 3, the peak values in AG faults match with phase A current and voltage peaks at 90 and 270 degrees, whereas the valleys, where no TW is detected, occur at 180 and 360 degrees. The healthy phases (B and C) present relevant first wavefront energy, indicating that there are traveling waves in health phases due to the mutual electromagnetic coupling effects between the phase conductors according to the line topology. However, the peak values of the healthy phases are smaller than the faulty one. The first wavefront energy of the zero-mode current also has significant values. The first wavefront of TWs induced by BG and CG faults present the same features, but with peaks and valleys in different fault inception angles according to Table I.

In a practical application, TWs induced by SLG faults are not detectable in specific fault inception angles. Therefore,

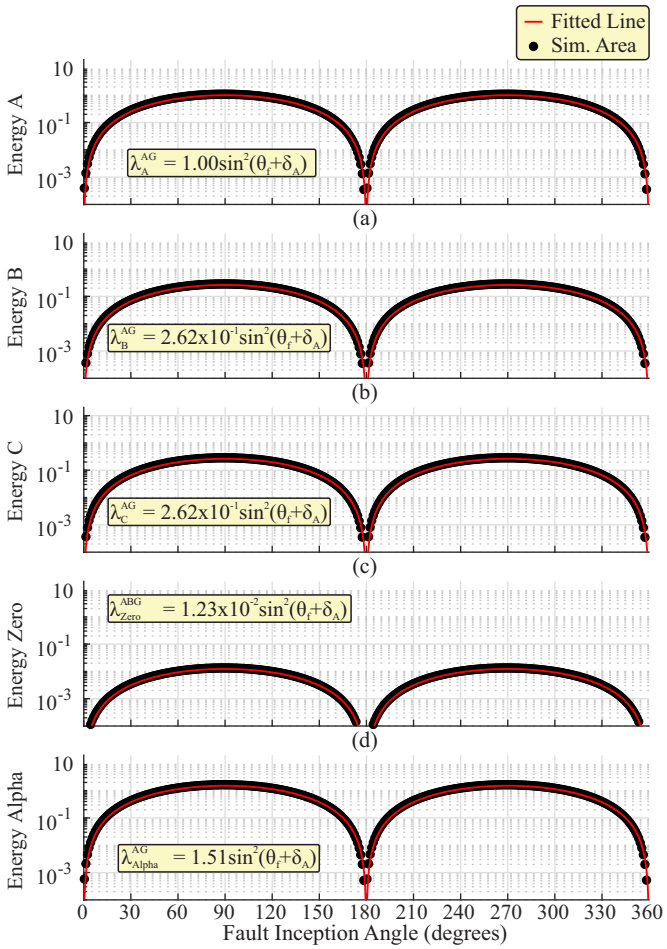

Fig. 3. First wavefront energy of AG faults: (a) phase A; (b) phase B; (c) phase C; (d) zero-mode; (e) alpha-mode.

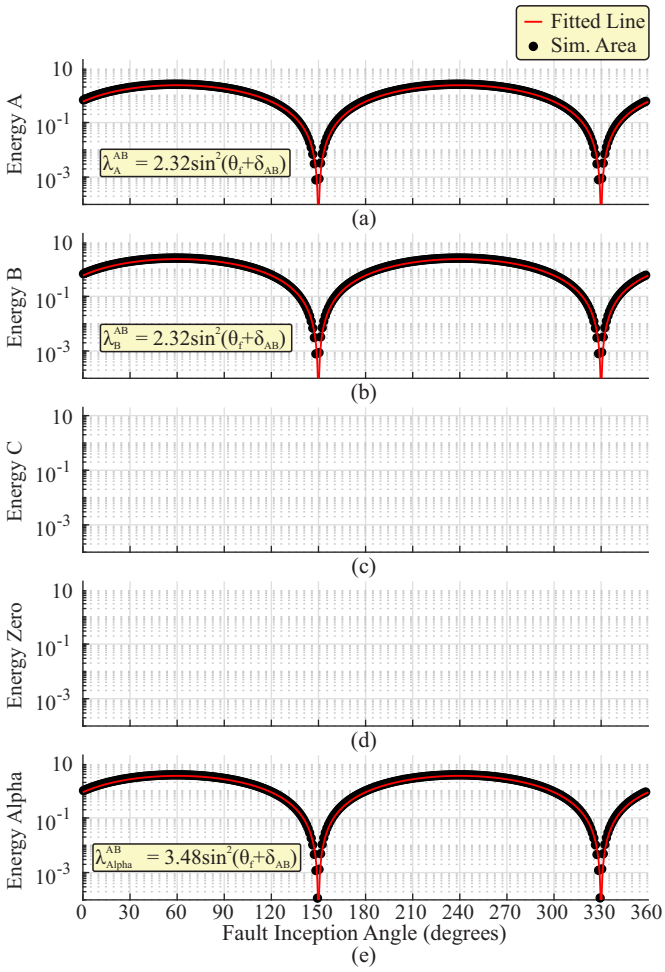

Fig. 4. First wavefront energy of AB faults: (a) phase A; (b) phase B; (c) phase C; (d) zero-mode; (e) alpha-mode.

TW-based detection, location, and protection methods will face problems in faults with specific fault inception angles.

C. Line-to-Line Faults

The first wavefront energy of the phase-A-to-phase-B fault (AB fault), in Fig. 4, have their peak values at 60 and 240 degrees, while the minimum values are at 150 and 330 degrees. The first wavefront energy in phase C, the healthy phase, is null even existing a mutual electromagnetic coupling with the faulty phases because the TWs in its conductor result from superposition between TWs with the same amplitude but opposite polarity in the faulty phases. As expected in the zero-mode, the first wavefront energy in any fault inception angle is despicable. The first wavefront of TWs induced by BC and CA faults present the same features, but with peaks and valleys in different fault inception angles according to Table I.

Line-to-line faults present more severe TWs than SLG faults because the fault circuit is powered by two phases instead of only one. For instance, the peak of alpha-mode first wavefront energy in AB faults has a magnitude higher than the energy peak in AG faults (Figs. 3 and 4).

In a practical application, TWs induced by LL faults are not detectable in specific fault inception angles. Therefore, TW-based detection, location, and protection methods will face problems in faults with specific fault inception angles.

D. Double Line-to-Ground Faults

According to Fig. 5, faulty phases in DLG faults present relevant TWs irrespective of the fault inception angle. In contrast, the healthy phase, the zero-mode, and the alpha-mode have no TWs in certain fault inception angles (Table I). The peak energy in all phases and alpha-mode TW takes place in different fault inception angles. However, the peak energy of the healthy phase takes place in the same fault inception angle of the zero-mode TW.

For fault inception angles around 150 and 330 degrees, TWs are dumped in phases A and B, whereas TWs in phase C, the healthy phase, are the most severe (Fig. 5). Therefore, depending on the fault inception angle, TWs of the healthy phase are more significant than the ones in the faulty phases.

For fault inception angles around 60 and 240 degrees, TWs of phase C, the healthy phase, and the zero-mode are irrelevant. Therefore, there is TWs only in faulty phases, such as in a LL fault. The first wavefront of TWs induced by BCG and CAG faults present similar features, but with peaks and

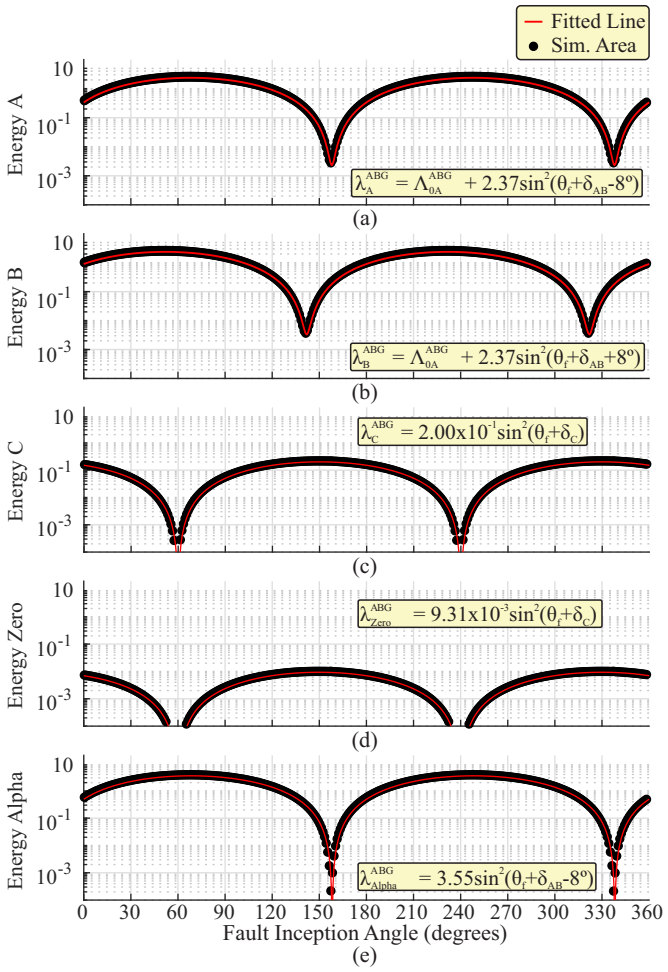

Fig. 5. First wavefront energy of ABG faults: (a) phase A; (b) phase B; (c) phase C; (d) zero-mode; (e) alpha-mode.

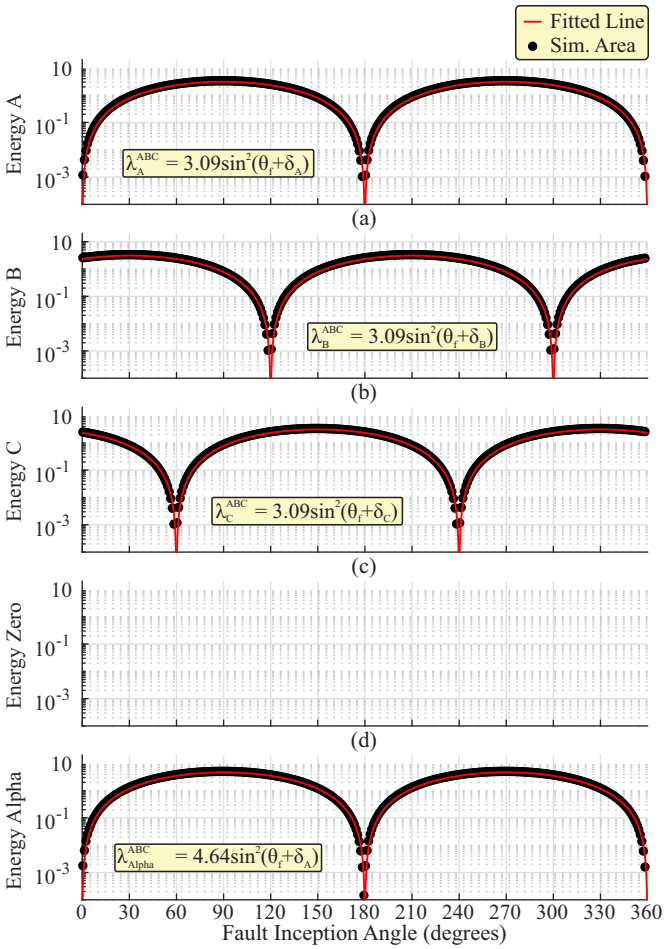

Fig. 6. First wavefront energy of three-phase faults: (a) phase A; (b) phase B; (c) phase C; (d) zero-mode; (e) alpha-mode.

valleys in different fault inception angles according to Table I.

In a practical application, TWs of phase currents induced by DLG faults are always detectable for any fault inception angle. Conversely, alpha-mode TWs, the most used by TW-based methods, are not detectable in specific fault inception angles (Fig. 5). Therefore, TW-based detection, location, and protection methods will face problems in faults with specific fault inception angles if alpha-mode TWs are used.

E. Three-phase faults

According to Fig. 6, the peak energy of TWs in all phase currents occurs in different fault inception angles. The same features are true for the valley values. As expected in the zero-mode, TWs in any fault inception angle are despicable. In addition, three-phase faults present the most severe TWs because the fault circuit are powered by all the phases (Figs. 3, 4, 5, and 6).

According to Fig. 6, TWs of a particular phase current are irrelevant for specific fault inception angles. Therefore, there are TWs only in two faulty phases in specific fault inception angles, such as in a LL fault. This feature would be a problem for TW-based fault classification methods.

In a practical application, TWs of phase currents induced by ABC faults are always detectable for any fault inception angle. Then, TW-based detection, location, and protection methods will not face problems related to the fault inception angle.

F. The Fault Resistance Influence in the Fault Inception Angle Properties

The aforementioned effects of the fault inception angle are true regardless the fault resistance. For instance, all the fault scenarios used to evaluate the effects of the fault inception angle in the traveling waves were one more time evaluated considering the fault resistance of R_f = 33 Ω instead of R_f = 0 Ω. Figs. 7, 8, 10, and 11 depict the first wavefront energy of AG, AB, ABG, ABC faults, respectively, by considering R_f = 33 Ω and the fault inception angle from 0 to 360^o. They were normalized with the maximum first wavefront energy of the AG fault: $\max[\lambda_A^{AG}] = 4.13 \times 10^{-4}$. This value is lower than that in the case of R_f = 0 Ω ($\max[\lambda_A^{AG}] = 5.36 \times 10^{-4}$) because the energy of traveling waves decreases when the fault resistance increases.

Comparing Figs. 7, 8, 10, and 11 to the related Figs. 3, 4, 5, and 6, despite different magnitude, the behavior of the first

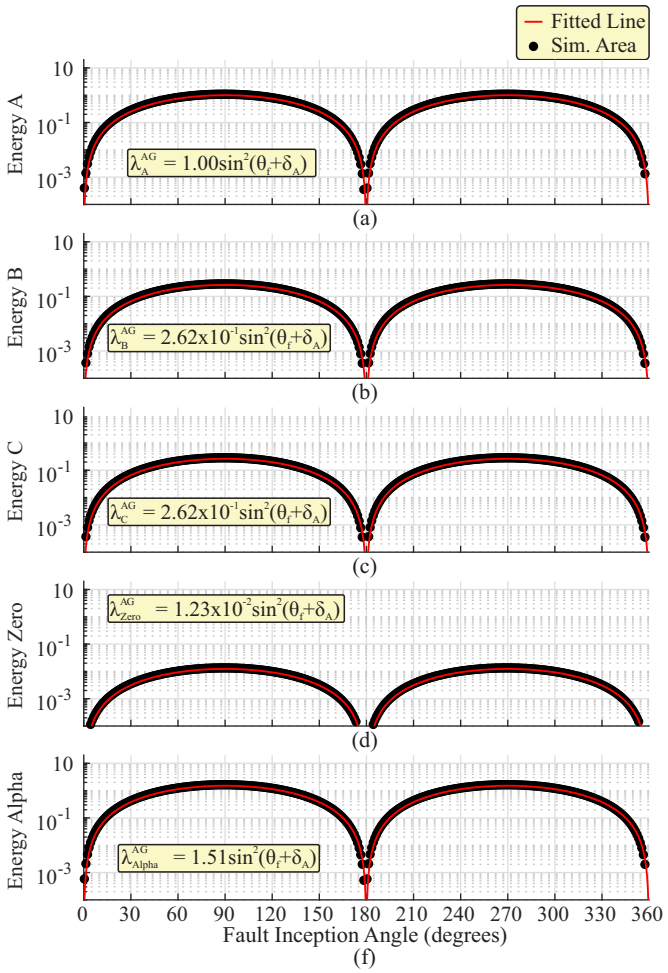

Fig. 7. First wavefront energy of AG faults (R_f = 33 Ω): (a) phase A; (b) phase B; (c) phase C; (d) zero-mode; (e) alpha-mode.

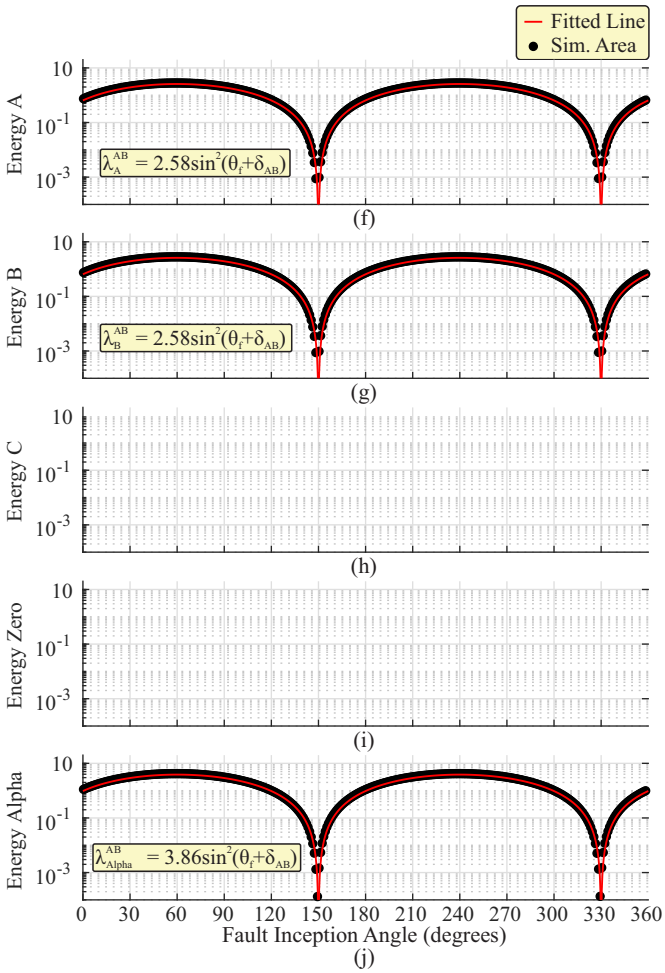

Fig. 8. First wavefront energy of AB faults, (R_f = 33 Ω): (a) phase A; (b) phase B; (c) phase C; (d) zero-mode; (e) alpha-mode.

wavefront energy related to fault inception angle remains the same regardless of the fault resistance. For instance, remains the same the fault inception angles which occur traveling waves with maximum and minimum energy, per type of fault. In addition, the energy of traveling waves remains a squared sinusoidal function with the fault inception angle.

VI. Experimental Assessment

The experimental setup shown in Fig. 9 was developed to analyze the influence of the fault inception angle in the first wavefront of TWs under conditions more similar to real transmission lines and validate the analysis accomplished with simulations. It is a three-phase version developed from the single-phase experimental setup presented in [9, 19]. It allows the generation, propagation, and measurement of TWs to assist the study of TWs in controlled scenarios. The experimental platform emulates a three-phase transmission line employing a one-kilometer polypropylene flex cable with four insulated copper wires with one square millimeter cross-sectional area.

As shown in Fig. 9, three insulated wires of the one-kilometer cable are connected to each of the three phases of the laboratory building main-grid at 127 V (RMS value): V_{SA}, V_{SB}, and V_{SC}. This connection point is called Bus I, where

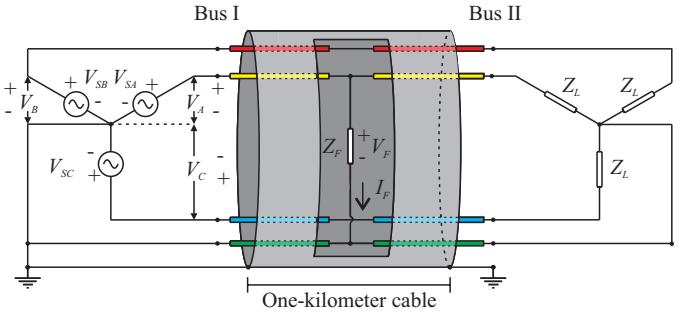

Fig. 9. Experimental setup.

the neutral wire is grounded. The other end of the cable is connected to a purely restive three-phase load with Z_L = 100 Ω. This last connection point is called Bus II, and it is not grounded. The fourth one-kilometer cable wire is connected to the neutral of the main grid and is also grounded at that point (Bus I). Its other end is connected to the neutral point of the three-phase ungrounded load.

Only voltages could be measured with a sampling frequency of 9.77 MHz. Fault resistors with resistance Z_F = 33 Ω were used in all fault configurations to avoid high fault current levels, which could damage the various elements of

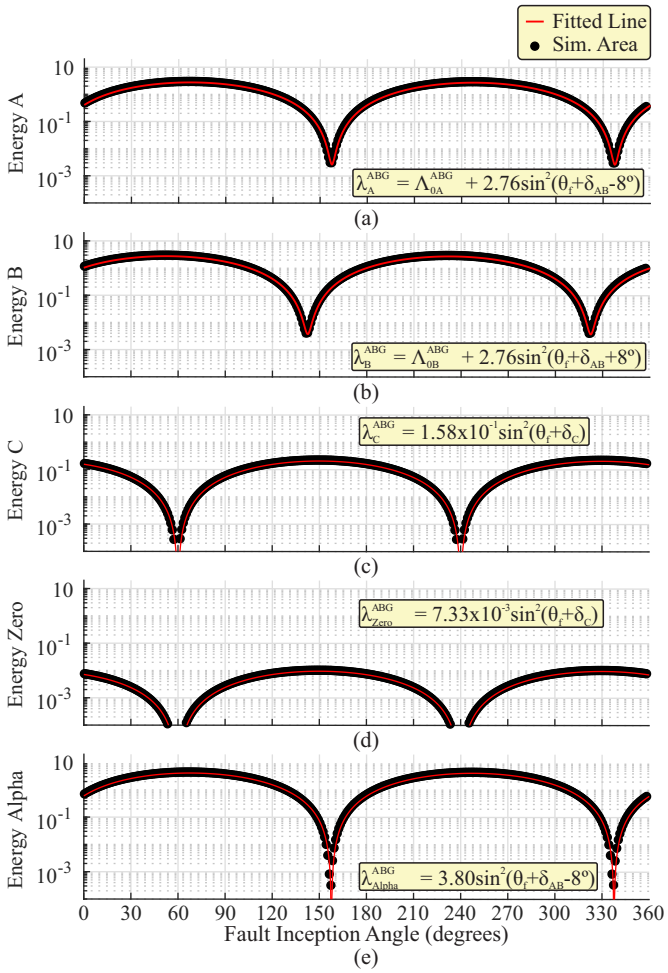

Fig. 10. First wavefront energy of ABG faults (R_f = 33 Ω): (a) phase A; (b) phase B; (c) phase C; (d) zero-mode; (e) alpha-mode.

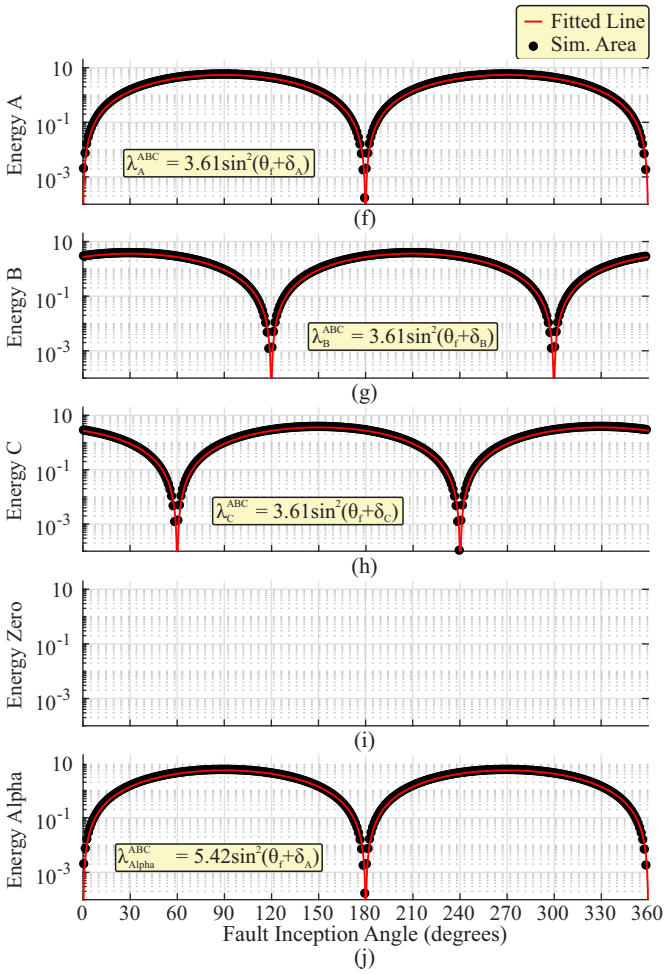

Fig. 11. First wavefront energy of three-phase faults (R_f = 33 Ω): (a) phase A; (b) phase B; (c) phase C; (d) zero-mode; (e) alpha-mode.

the experimental setup. The fault application is controlled manually through a push-button connected to switches. Since the switches are electromechanical, there is a significant delay between them while switching, which compromises the TW analysis. Therefore, only SLG faults could be applied in this experimental setup.

A thorough description of the experimental setup regarding electromagnetic isolation, signal measurement, frequency bandwidth response, data acquisition and analysis, strategy for fault application, and the detailed evaluation of the TWs propagation can be found in [9, 19].

Fig. 12 depicts the first wavefront energy of TWs induced by AG faults experimentally. They were normalized based on the maximum first wavefront energy of the phase-A voltage: $\max[\lambda_A^{AG}] = 1.48\times10^{-5}$. By comparing the features of experimental TWs in Fig. 12 with the TWs of simulated AG faults in Fig. 3, then both fitted curves have peak values and valleys at the same fault inception angle, both present the same equation format, and the maximum value of the first wavefront energy of the faulty phase is greater than the ones of the healthy phases. Therefore, even using different system topologies, the experimental and simulated results fitted well, demonstrating the validity of the presented TW features.

VII. Conclusions

This work presented the influence of the fault inception angle over the first wavefront of traveling waves considering realistic computational simulations and experimental setup. Some TW features are standard in all fault types, whereas some TW features strongly change with the fault type. These features are essential for designing TW-based detection, location, and protection methods. In summary, the following TW features are highlighted:

- The energy of TWs changes with the fault inception angle according to a squared sinusoidal function, where TWs present maximum and minimum values at specific fault inception angles according to the type of fault.
- TWs are not detectable in specific fault inception angles in SLG and LL faults, whereas they are detectable for DLG and three-phase faults regardless the fault inception angle. Therefore, TW-based detection, location, and protection methods will face problems in SLG and LL faults with specific fault inception angles.
- The detection of TWs based on the alpha-mode TWs will be difficult in DLG faults with specific fault inception angles, whereas the detection based on phase-mode TWs would not be a problem.

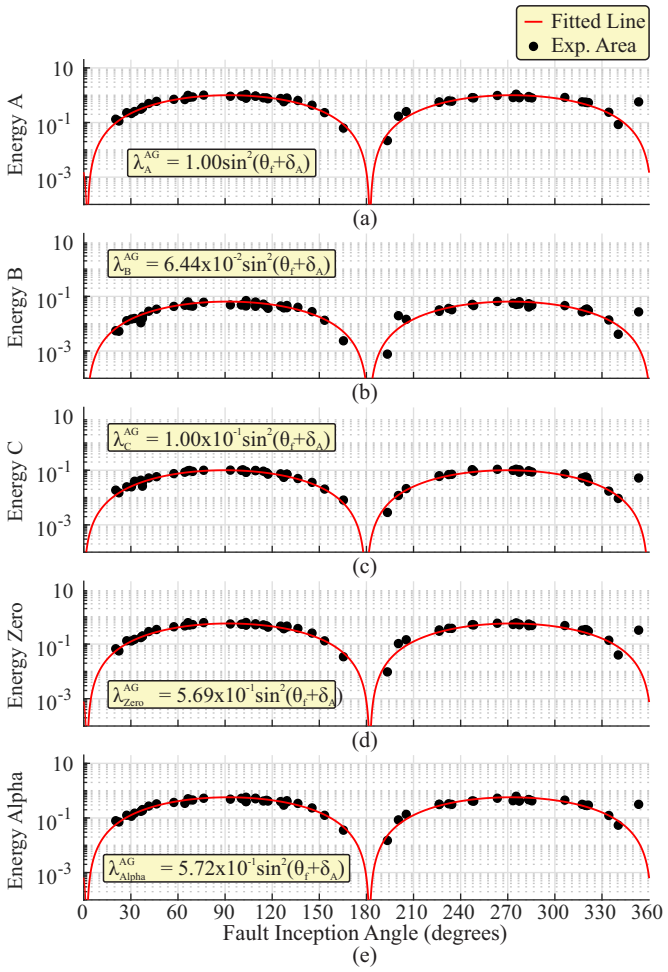

Fig. 12. First wavefront energy areas of AG experimental fault: (a) phase A; (b) phase B; (c) phase C; (d) zero-mode; (e) alpha-mode.

- TWs of DLG and three-phase faults present features similar to a LL fault in specific fault inception angles, which would be a concern to a TW-based fault classification.

References

[1] Y. G. Paithankar and S. R. Bhide. *Fundamentals of power system protection*. PHI Learning Pvt. Ltd., 2010.

[2] III E. O. Schweitzer, B. Kasztenny, A. Guzmán, V. Skendzic, and M. V. Mynam. Speed of line protection - can we break free of phasor limitations? In *2015 68th Annual Conference for Protective Relay Engineers*, 2015.

[3] P. Jafarian and M. Sanaye-Pasand. A traveling-wave-based protection technique using wavelet/pca analysis. *IEEE Transactions on Power Delivery*, 25(2):588–599, 2010.

[4] F. B. Costa, A. Monti, F. V. Lopes, K. M. Silva, P. Jamborsalamati, and A. Sadu. Two-terminal traveling-wave-based transmission-line protection. *IEEE Transactions on Power Delivery*, 32(3):1382–1393, 2017.

[5] S. Lin, Z. Y. He, X. P. Li, and Q. Qian. Travelling wave time?frequency characteristic-based fault location method for transmission lines. *IET Generation, Transmission & Distribution*, 6(8):764–772, 2012.

[6] R. L. S. França, F. C. Silva Jr., T. R. Honorato, J. P. G. Ribeiro, F. B. Costa, F. V. Lopes, , and K. Strunz. Traveling wave-based transmission line earth fault distance protection. *IEEE Transactions on Power Delivery*, pages 1–1, 2020.

[7] N. Davydova and G. Hug. Travelling wave protection with disturbance classification for distribution grids with distributed generation. In *International Conference on Developments in Power System Protection*, 2018.

[8] X. Dong, W. Kong, and Tao Cui. Fault classification and faulted-phase selection based on the initial current traveling wave. *IET Generation, Transmission & Distribution*, 24(2): 552–559, 2009.

[9] F. B. Costa, F. V. Lopes, K. M. Silva, K. M. C. Dantas, R. L. S. França, M. M. Leal, and R. L. A. Ribeiro. Mathematical development of the sampling frequency effects for improving the two-terminal traveling wave-based fault location. *International Journal of Electrical Power & Energy Systems*, 115, 2020.

[10] X. Dong, S. Luo, S. Shi, B. Wang, L. Ren, and F. Xu. Implementation and application of practical traveling-wave-based directional protection in uhv transmission lines. *IEEE Trans. Power Delivery*, 31(1):294–302, 2016.

[11] R. Aguilar, F. Peréz, and Orduña E. High-speed transmission line protection using principal component analysis, a deterministic algorithm. *IET Generation, Transmission & Distribution*, 5(7):712–719, 2011.

[12] F. Namdari and M. Salehi. High-speed protection scheme based on initial current traveling wave for transmission lines employing mathematical morphology. *IEEE Transactions on Power Delivery*, 32(1):246–253, 2017.

[13] F. V. Lopes, Jr. D. Fernandes, and W. L. A. Neves. A traveling-wave detection method based on park's transformation for fault locators. *IEEE Transactions on Power Delivery*, 28 (3):1626–1634, 2013.

[14] P. Jafarian and M. Sanaye-Pasand. A traveling-wave-based protection technique using wavelet/pca analysis. *IEEE Transactions on Power Delivery*, 25(2):588–599, 2010.

[15] F. Lopes, E. Leite, J. P. Ribeiro Jr., L. Lopes, A. Piardi, R. Otto, and W. Neves. Using the differentiator-smoother filter to analyze traveling waves on transmission lines: Fundamentals, settings and implementation. In *International Conference on Power Systems Transients*, 2019.

[16] Schweitzer Engineering Laboratories SEL. Ultra-high-speed transmission line relay traveling-wave fault locator high-resolution event recorder. 2017.

[17] F. B. Costa. Fault-induced transient detection based on real-time analysis of the wavelet coefficient energy. *IEEE Transactions on Power Delivery*, 29(1):140–153, Feb 2014. ISSN 0885-8977. doi: 10.1109/TPWRD.2013.2278272.

[18] F. B. Costa and J. Driesen. Assessment of voltage sag indices based on scaling and wavelet coefficient energy analysis. *IEEE Transactions on Power Delivery*, 28(1):336–346, Jan 2013. ISSN 0885-8977. doi: 10.1109/TPWRD.2012.2218626.

[19] R. L. S. França, M. M. Leal, M. S. R. Leal, M. R. Marques, F. B. Costa, and R. L. A. Ribeiro. Experimental test bench for traveling-wave-based methods evaluations. In *International Conference on Power Systems Transients*, 2019.